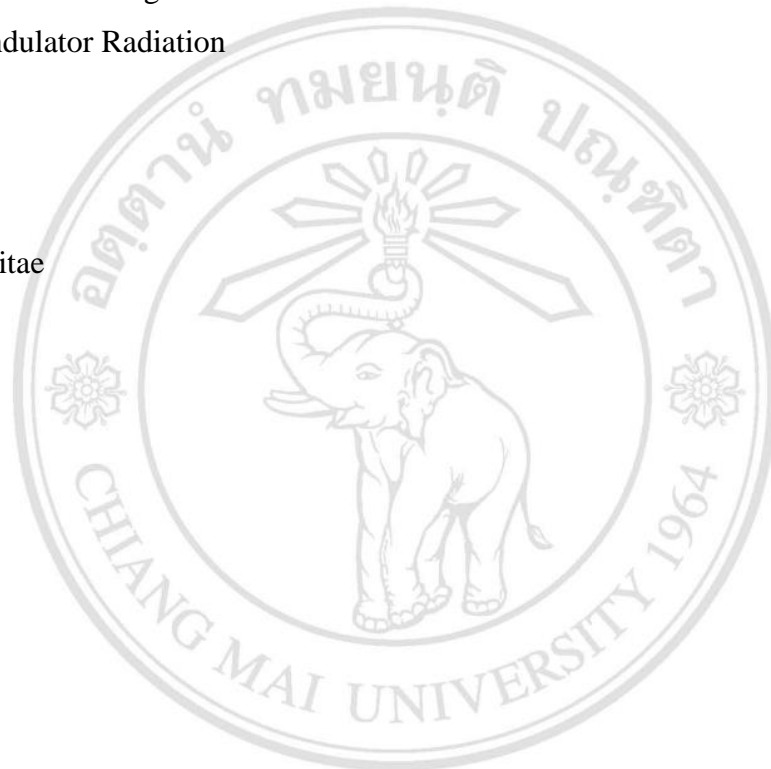


CONTENTS

	Page
Acknowledgement	iii
Abstract in Thai	iv
Abstract in English	v
List of Tables	x
List of Figures	xi
Chapter 1 Introduction	1
Chapter 2 Theory and Principle	6
2.1 Electron Source of the PBP-CMU Linac System	6
2.2 Travelling-wave Linear Accelerator	11
2.3 Charged Particle Motion in Electromagnetic Fields	12
2.3.1 Steering Magnet	15
2.3.2 Quadrupole Magnet	16
2.3.3 Alpha Magnet	17
2.4 Electron Beam Parameters	19
2.4.1 Time Structure	19
2.4.2 Beam Currents	19
2.4.3 Electron Beam Energy and Energy Spread	20
2.4.4 Transverse Beam Emittance	20
2.5 Space Charge Effects	22
2.6 Beam Dynamic Simulation	22
2.6.1 PARMELA	23
2.6.2 ELEGANT	24
2.7 Undulator Magnet and Undulator Radiation	25
2.7.1 Electron Motion in Undulator Magnetic Field	25

2.7.2 Undulator Radiation	28
2.7.3 Angular Flux Distribution of Undulator Radiation	29
2.7.4 Spectral Power in Central Cone	32
2.7.5 Coherent Radiation	34
2.7.6 Radiation Brightness	37
2.8 Transition Radiation	38
Chapter 3 Start-to-End Beam Dynamics Simulation	40
3.1 Electron Beam Dynamics Simulation inside the RF-gun	42
3.2 Beam Dynamics Simulation from RF-gun Exit to Alpha Magnet Entrance (GTA)	46
3.3 Beam Dynamics Simulation from Alpha Magnet to Experimental Station (ATE)	53
3.3.1 Beam Dynamics Simulation in Alpha Magnet	53
3.3.2 Optimization of Longitudinal Mesh for Simulation in ATE Section	56
3.3.3 Optimization of Alpha Magnet Gradient	57
3.3.4 Optimization of Linac RF Phase	64
3.3.5 Optimization of Energy Filtering	69
3.4 Comparison of Measured Electron Beam Properties and Simulation Results	76
Chapter 4 Study on Undulator Radiation	81
4.1 Undulator Magnet	81
4.1.1 Choice of Undulator Period Length and Undulator Parameter	81
4.1.2 Prototype of Electromagnetic Undulator Magnet	83
4.1.3 Undulator Magnet with 30 Periods	86
4.2 Undulator Radiation	88
4.2.1 Radiation Wavelength	88
4.2.2 Radiation Average Power vs. Electron Beam Energy	90
4.2.3 Radiation Average Power vs. Electron Bunch Length	92
4.2.4 Radiation Average Power vs. Electron Bunch Charge	94

4.2.5 Comparison between Measurement and Simulation Results	96
4.2.6 Comparison between Undulator Radiation and Transition Radiation	98
Chapter 5 Conclusion	101
5.1 Beam Dynamics Simulation	101
5.2 Undulator Magnet	103
5.3 Undulator Radiation	104
References	106
Appendix	110
Curriculum Vitae	111



ลิขสิทธิ์มหาวิทยาลัยเชียงใหม่
 Copyright© by Chiang Mai University
 All rights reserved

LIST OF TABLES

		Page
Table 1.1	Measured beam parameters of the PBP-CMU Linac in 2011.	3
Table 3.1	The electric field parameters of the PBP-CMU gun obtained from the results of the 3D MWS model.	43
Table 3.2	Comparison of particle distribution formats for programs PARMELA and ELEGANT.	54
Table 3.3	Operating parameters for 3 considered cases.	76
Table 3.4	Measured properties of electron beam after accelerating in the linac.	77
Table 3.5	Operating parameters and simulated electron beam properties at the experimental station for simulation of Case 2 and Case 3.	80
Table 4.1	Specifications of the electromagnetic undulator for generation of THz radiation at the PBP-CMU Linac Laboratory.	87

LIST OF FIGURES

		Page
Figure 1.1	Electromagnetic spectrum diagram.	1
Figure 1.2	Schematic drawing showing the components of the PBP-CMU Linac system.	2
Figure 2.1	Outside and inside structures of the three-dimensional model of the PBP-CMU RF-gun.	6
Figure 2.2	Electromagnetic field directions in the TM010-mode pillbox cavity.	7
Figure 2.3	Longitudinal electric field (E_z) inside the TM010-mode pillbox cavity as a function of the radius (r) and the longitudinal distance (z).	8
Figure 2.4	Disk-loaded traveling-wave structure with waveguide input port.	11
Figure 2.5	Schematic picture shows the $2\pi/3$ operating mode of traveling-wave linac acceleration. The electric field has a phase shift of $2\pi/3$ per cavity.	11
Figure 2.6	Actual path of a positive charge e with respect to the reference trajectory.	13
Figure 2.7	Picture of the steering magnet at the PBP-CMU Linac Laboratory (left) and a schematic structure of the steering magnet illustrating the magnetic field lines, which can be employed as a vertical bending magnet (right).	15
Figure 2.8	Cross sectional structure of a quadrupole magnet.	16
Figure 2.9	Electron trajectories in the alpha magnet with energy slits.	18
Figure 2.10	Time structure of the electron beam modified from the reference.	19
Figure 2.11	Phase space ellipse with betatron function of an electron bunch.	21
Figure 2.12	Elliptical model of macro-particles in an electron bunch (left) and the rectangular cross-section of the elliptical model (right).	24

Figure 2.13	Schematic picture illustrates the sinusoidal trajectory of the electron along the undulator axis with the emitted radiation.	26
Figure 2.14	Electron moving path in the undulator magnetic field with its radiation cone.	27
Figure 2.15	The interference effect of the emitted radiation produced from an electron moving in the undulator magnetic field modified from the reference.	28
Figure 2.16	Configuration of the undulator radiation with the observation point.	30
Figure 2.17	Characteristics of the lineshape function $L_n(\lambda_r)$ for the first harmonic.	31
Figure 2.18	The radiation pattern of odd harmonics in the moving frame (left) and the laboratory frame (right).	32
Figure 2.19	The radiation pattern of even harmonics in the moving frame (left) and the laboratory frame (right).	33
Figure 2.20	Transition radiation of an electron travelling through boundary between vacuum and a perfect conductor.	39
Figure 3.1	Flowchart of simulation algorithms of beam dynamics simulation.	41
Figure 3.2	Electric field vectors inside the RF-gun for the horizontal plane (left) and for the vertical plane (right).	43
Figure 3.3	Dependency of average and maximum energy (vertical left axis) and energy spread (vertical right axis) of electron beam at the gun exit as a function of average electric field at the center of the full cell.	44
Figure 3.4	RMS transverse beam size and divergence as a function of the average electric field at the full-cell center (left). The rms emittance and the micro-bunch charge of electron beam exiting the RF-gun as a function of the average electric field at the full-cell (right).	44

Figure 3.5	Contour plots of transverse beam distribution (x-y), longitudinal phase space distribution (E_k -t) with histogram of the number of macro-particles at the RF-gun exit and transverse phase space distributions (x-x' and y-y').	45
Figure 3.6	Transverse distribution (x-y), energy spectrum and transverse phase space distributions (x-x' and y-y') at the RF-gun exit. Different colors in the plots represent different particle energies.	46
Figure 3.7	Three-dimensional electron beam distribution at the RF-gun exit.	46
Figure 3.8	RMS transverse beam size along the GTA section for different simulation conditions. The data points in the graphs represent the positions of the RF-gun exit, ST1, Q1, Q2, Q3, ST2, and the alpha magnet entrance, respectively.	48
Figure 3.9	Divergence of electron beam along the GTA beamline for different simulation conditions.	48
Figure 3.10	RMS transverse emittance along the GTA section for 3 conditions of beam dynamic simulation.	49
Figure 3.11	Average kinetic energy and energy spread along the GTA section for 3 cases of beam dynamic simulations.	50
Figure 3.12	Electron bunch charge at the positions of the elements along the GTA part for different conditions of beam dynamic simulation.	50
Figure 3.13	Transverse beam distributions (x-y), the energy-time phase space (E_k -t) with histogram and transverse phase space distributions (x-x' and y-y') of electron bunch at the alpha magnet entrance. Different colors in the plots represent different particle intensities in arbitrary unit.	51
Figure 3.14	Transverse distribution (x-y), energy spectrum and transverse phase space distributions (x-x' and y-y') with energy classification at the alpha magnet entrance. Different colors in the plots represent the particles with different energies.	52
Figure 3.15	Three-dimensional electron beam distribution with energy classification at the alpha magnet entrance.	52

Figure 3.16	Contour plots of transverse beam distribution (x-y), the energy-time phase space (E_k -t) with histogram and transverse phase space distributions (x-x' and y-y') of electron beam at the alpha magnet exit for the magnetic field gradient of 328 G/cm. Different colors in the plots represent different particle intensities in arbitrary unit.	55
Figure 3.17	Transverse distribution (x-y), energy spectrum and transverse phase space distributions (x-x' and y-y') with energy classification at the alpha magnet exit for the magnetic field gradient of 328 G/cm. Different colors in the plots represent the particles with different energies.	55
Figure 3.18	Three-dimensional electron beam distribution with energy classification at the alpha magnet exit for the magnetic field gradient of 328 G/cm. Different colors in the plots represent the particles with different energies.	56
Figure 3.19	Bunch length, rms transverse emittance and energy spread of electron beam at the experimental station for different numbers of longitudinal mesh interval.	57
Figure 3.20	Energy-time distributions at the alpha magnet exit for magnetic field gradients of 100 - 700 G/cm.	58
Figure 3.21	Histograms of the electron bunches at the alpha magnet exit for alpha magnet gradients of 100, 300, 500, 700 G/cm.	58
Figure 3.22	RMS transverse beam size, divergence and rms transverse emittance at the alpha magnet exit as a function of the alpha magnet gradient.	59
Figure 3.23	Transverse distribution (x-y) and transverse phase space (x-x' and y-y') of electron bunches exiting from the alpha magnet for the alpha magnet gradients of 100, 200, 300, and 400 G/cm.	60
Figure 3.24	Longitudinal phase space distributions of electron bunches at the linac entrance for alpha magnet gradients of 100 - 700 G/cm.	60

Figure 3.25	Longitudinal phase space distributions of electron bunches arriving at the experimental station for alpha magnet gradients of 100 - 700 G/cm.	61
Figure 3.26	Energy-time distributions and histograms of electron bunches at the experimental station for alpha magnet gradients of 100 - 600 G/cm.	62
Figure 3.27	RMS and Gaussian fitting bunch lengths at the experimental station for alpha magnet gradients of 100 - 400 G/cm. The right vertical axis shows the R-squared value of the Gaussian fitting for each gradient.	63
Figure 3.28	FWHM bunch length (left vertical axis) and micro-bunch charge (right vertical axis) at the experimental station for alpha magnet gradients of 100 - 400 G/cm.	63
Figure 3.29	3D particle distribution (top left), transverse beam distribution (top right), energy spectrum (bottom left) and energy-time phase space with histogram (bottom right) at the linac entrance for alpha magnet gradient of 300 G/cm without energy filter.	64
Figure 3.30	Average and maximum kinetic energies (left) and rms transverse emittance (right) of electron bunches, which are accelerated along the linac with a given RF phase of 90° for alpha magnet gradients of 200 G/cm and 400 G/cm.	65
Figure 3.31	Average beam energy and energy spread at the experimental station as a function of alpha magnet gradient for the linac phases of 70° , 80° , 90° , 100° , and 110° .	66
Figure 3.32	RMS bunch length, bunch length from Gaussian fitting (left) and R-squared value of the Gaussian fitting (right) at the experimental station as a function of the alpha magnet gradient for the linac RF phases of 70° - 110° .	67
Figure 3.33	FWHM bunch length and electron bunch charge at the experimental station as a function of the alpha magnet gradient for the linac phases of 70° - 110° .	67

Figure 3.34	RMS, Gaussian fitting and FWHM bunch lengths of electron beams at experimental station versus linac RF phase in the range of 80° - 100° (left) and the relation between the optimal gradient of the alpha magnet and the linac RF phase (right).	68
Figure 3.35	Transverse beam distributions (x-y), the energy-time phase space (E_k -t) with histogram and transverse phase space (x-x' and y-y') at the alpha magnet exit for the linac RF phase of 87° and the alpha magnet gradient of 209 G/cm without energy filter.	70
Figure 3.36	3D electron beam distribution, energy spectrum and transverse phase space distributions (x-x' and y-y') at the alpha magnet exit for the linac RF phase of 87° and the alpha magnet gradient of 209 G/cm without energy filter.	70
Figure 3.37	RMS transverse beam emittance, micro-bunch charge, average kinetic energy and energy spread of electron beam at the alpha magnet exit as a function of the minimum energy cut by using the energy slit inside the alpha magnet.	71
Figure 3.38	Transverse beam distributions at the linac exit for energy filter with different minimum energies.	72
Figure 3.39	Energy-time phase spaces and histograms of macro-particles at the experimental station for energy filters in the range of 2.0 to 2.4 MeV compared to the case of without energy filter.	73
Figure 3.40	Longitudinal distributions and particle histograms of electrons concentrating in the head of the bunch at the experimental station for the energy filter with minimum energies of 2.1, 2.2, 2.3, and 2.4 MeV.	74

- Figure 3.41 Transverse distribution, longitudinal phase space distribution with histogram of macro-particle number and transverse phase spaces of electron bunch at the experimental station for optimal operating parameters, which the linac RF phase is 87° , the alpha magnet gradient is 209 G/cm and the minimum energy filter is 2.1 MeV. Different colors in the plots represent different particle intensities in arbitrary unit. 75
- Figure 3.42 Transverse distribution, energy spectrum and transverse phase space distributions at the experimental station for optimal operating conditions, which the linac RF phase is 87° , the alpha magnet gradient is 209 G/cm and the minimum energy filter is 2.1 MeV. Different colors in the plots represent the particles with different energies. 75
- Figure 3.43 Three-dimensional electron beam distribution at the experimental station for optimal operating parameters, which the linac RF phase is 87° , the alpha magnet gradient is 209 G/cm and the minimum energy filter is 2.1 MeV. 76
- Figure 3.44 Measured kinetic energy and bunch charge of the electron beam after accelerating in the linac by using a dipole magnet and a Faraday cup. 77
- Figure 3.45 Measured electron bunch length at the experimental station as a function of the alpha magnet gradient. 77
- Figure 3.46 Contour plots of transverse beam distribution (x - y), longitudinal phase space (E_k - t) with histogram of the number of macro-particles and transverse phase space distributions (x - x' and y - y') at the experimental station for simulated beam of Case 2. 78
- Figure 3.47 Transverse distribution (x - y), energy spectrum and transverse phase space distributions (x - x' and y - y') at the experimental station for simulated beam of Case 2. Different colors in the plots represent the particles with different energies. 79

Figure 3.48	Three-dimensional electron beam distribution at the experimental station for simulated beam of Case 2. Different colors in the plots represent the particles with different energies.	79
Figure 4.1	Schematic layout of the future accelerator system at the PBP-CMU Linac Laboratory. Dimensions of all components are not scaled.	81
Figure 4.2	Undulator period length as a function of undulator parameter for electron energies of 10, 12, 15 and 20 MeV.	82
Figure 4.3	3D RADIA model of undulator prototype with 6 periods (left) and the actual undulator prototype (right).	83
Figure 4.4	Ideal and measured magnetic field distributions on the mid plane along the undulator axis at an excitation current of 1 A.	84
Figure 4.5	Angular displacement or the deflecting angle of 10 MeV electron along the undulator axis for ideal periodic and measured magnetic fields.	84
Figure 4.6	Horizontal displacement of 10 MeV electron beam along the undulator axis for ideal periodic and measured magnetic fields.	85
Figure 4.7	Calculated angular flux density as a function of photon energy with electron energy of 10 MeV for ideal periodic and measured magnetic fields.	86
Figure 4.8	3D RADIA model of the electromagnetic undulator with 30 periods.	86
Figure 4.9	Ideal magnetic field distribution along the longitudinal distance of the undulator magnet with 30 periods.	87
Figure 4.10	Electron displacement of 10 MeV electron beam traveling through an ideal periodic magnetic field of the 30 period undulator.	87
Figure 4.11	Angular flux density as a function of photon energy with electron energy of 10 MeV for ideal periodic magnetic field of 30 period undulator.	88
Figure 4.12	Undulator radiation wavelength as a function of undulator parameter for electron energies of 5, 7, 10, 15 and 20 MeV.	89

Figure 4.13	Electron bunch length versus the bunch form factor for radiation wavelength of 100, 500, and 1000 μm .	90
Figure 4.14	Radiated average power of the first three harmonics of undulator radiation as a function of radiation wavelength for the electron beam with measured properties shown in Table 3.4.	91
Figure 4.15	Spectral average power at fundamental harmonic of the undulator radiation from 9.81 MeV electron beam with the undulator parameter from $K = 0.3$ to $K = 1$.	91
Figure 4.16	Spectral average power of undulator radiation at fundamental harmonic for electron beam energies of 8, 10 and 12 MeV without limitation of undulator parameter (left) and with the undulator parameter range of $K = 0.3$ to $K = 1$ (right).	92
Figure 4.17	Spectral power of undulator radiation at fundamental harmonic for electron beam with the bunch lengths of 45, 65, 85, 105, and 200 μm .	93
Figure 4.18	Radiated spectral power at fundamental harmonic for the electron beams with different bunch lengths for undulator parameters of $K = 0.3$ to $K = 1$.	94
Figure 4.19	Radiated power for the first three harmonics of undulator radiation produced from electron bunch charges of 20, 60, 100 pC with the undulator parameter in the range of $K = 0.3$ to $K = 1$. The radiation with wavelengths longer than 90 μm is the coherent radiation, while the radiation with wavelengths shorter than 90 μm has only the incoherent contribution.	95
Figure 4.20	Spectral power for the undulator radiation at the fundamental harmonic for different electron bunch charges with undulator parameters in the range of $K = 0.3$ to $K = 1$. The radiation with wavelengths longer than 90 μm is the coherent radiation, while the radiation with wavelengths shorter than 90 μm has only the incoherent contribution.	96

Figure 4.21	Radiated power of the undulator radiation at fundamental harmonic for electron beam properties in cases of measurement, simulation with measurement conditions, and simulation with optimal operating parameters.	97
Figure 4.22	Radiated power of the undulator radiation at the first three harmonics with undulator parameters in the range of $K = 0.3$ to $K = 1$ for three considered cases.	98
Figure 4.23	Comparison of radiation average powers of the undulator radiation (UR) and the transition radiation (TR) for electron beams with the properties obtained from the measurement (Table 3.4).	99
Figure 4.24	Average powers of undulator radiation (UR) and transition radiation (TR) for electron beams with the properties obtained from the simulation for the measurement conditions.	99
Figure 4.25	Average powers of undulator radiation (UR) and transition radiation (TR) for electron beams with the properties obtained from the simulation for the optimal operating parameters.	100